PHYSICAL REVIEW LETTERS

☞

Precursors to Splashing of Liquid Droplets on a Solid Surface

Shreyas Mandre,* Madhav Mani, and Michael P. Brenner

School of Engineering and Applied Sciences, Harvard University, Cambridge, Massachusetts 02138, USA
(Received 5 September 2008; published 31 March 2009)

A high velocity impact between a liquid droplet and a solid surface produces a splash. Classical work traced the origin of the splash to a thin sheet of fluid ejected near the impact point. Mechanisms of sheet formation have heretofore relied on initial contact of the droplet and the surface. We demonstrate that, neglecting intermolecular forces between the liquid and the solid, the liquid does not contact the solid, and instead spreads on a very thin air film. The interface of the droplet develops a high curvature and emits capillary waves.

The impact of a droplet hitting a solid surface produces a splash. Despite nearly a century of study [1], the mechanisms underlying splashing are poorly understood. Empirical splash thresholds have been developed [2–5] for the critical velocity of impact as a function of surface tension, density, viscosity, and the surface roughness. Recently, Xu, Zhang, and Nagel [6] demonstrated that when the ambient air pressure decreases below a threshold, splashing is suppressed and instead the droplet spreads smoothly onto the solid surface.

Previous observations [7,8] discovered that splashing is always preceded by the ejection of a thin fluid sheet near the contact point, the breakdown of which causes the splash. The most compelling rationale for sheet formation relies on the droplet contacting the surface. After a time t, a droplet of radius R falling at velocity V has penetrated the solid surface at a distance Vt. The radius of the wetted area is $r_{wet} = \sqrt{2RVt}$, giving $dr_{wet}/dt = \sqrt{RV/2t}$. The thin liquid sheet is said to originate when the velocity of the impact "rim" slows below the liquid sound velocity, causing an abrupt pressure increase at the contact line [7,9].

Observations show a liquid sheet launched into the air and not along the surface, as the model predicts. Moreover, a liquid film moving quickly along a solid surface experiences enormous frictional forces which strongly resist deformation of the sheet off the solid surface. This issue, coupled with the role of ambient air [6], led us to the hypothesis that the liquid sheet might originate due to the interaction of the liquid with the intervening gas layer *before* the droplet contacts the solid surface.

The goal of this Letter is therefore to study the approach of a droplet to a solid surface through an intervening gas layer, to search for potential fluid mechanical mechanisms for sheet generation before contact. We demonstrate a rich set of phenomena before a droplet contacts a solid surface. Even at very high impact speeds, the combined action of the gas layer and liquid surface tension allows the liquid to avoid contact; instead the droplet spreads on a very thin film of air and emits capillary waves.

We consider a droplet of radius R approaching a solid surface with velocity V. Close to the surface, viscous and pressure forces in the gas [with density $\rho(x, t)$] decelerate the droplet, deforming the interface, $h(x, t)$. We model this by coupling flow in an incompressible, inviscid liquid cylinder to a gas layer underneath. Parameters describing the system include the viscosity of the gas μ, the liquid density ρ_l, the liquid surface tension σ, and the equation of state of the gas, $P = P_0(\rho/\rho_0)^\gamma$, where P_0 is the ambient pressure of the gas at density ρ_0 and γ is a constant. Under the compressible lubrication approximation [10] the gas film deforms according to

$$12\mu(\rho h)_t = (\rho h^3 p_x)_x. \tag{1}$$

The equation for the droplet balances the acceleration of the liquid interface with the vertical pressure gradient: $\rho_l h_{tt} = -p_y^{\text{liquid}}$. The liquid pressure is related to the gas pressure using the Gibb's condition $p^{\text{liquid}} = p + \sigma h_{xx}$. We can further relate p_y to p_x [11], resulting in the equation
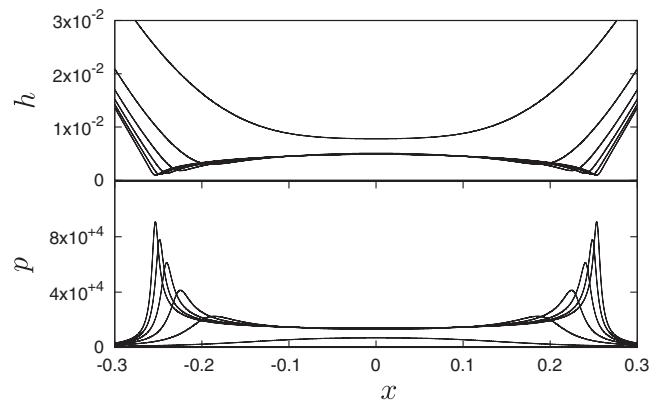

FIG. 1. Early stages in the evolution of a droplet impacting a solid surface (corresponding to dimensionless parameters $\epsilon = 5 \times 10^{-3}$, $\gamma = 1.4$, see text for definitions). The top [bottom] panel shows a snapshot of $h(x, t)$ [$p(x, t)$] as the drop approaches contact. Note the pressure maximum causes a dimple in the interface, and later splits into two maxima.

$$\rho_l h_{tt} = \mathcal{H}[p_x + \sigma h_{xxx}], \qquad (2)$$

where $\mathcal{H}$ is the Hilbert transform. The interface is initially assumed to be at $y = h_0 + x^2/2R$, where h_0 is a large distance from the wall and having a prescribed constant speed $h_t = -V$. The numerical simulations reported below solve this set of equations using a finite difference scheme [12] for (1) and a spectral decomposition [13] for (2). The validity of the model has been discussed in detail elsewhere [11], which we have modified to include the compressibility of the gas. The requisite conditions for the model are $\mu \ll \rho_l VR$ and $\mu V \ll RP_0$. A very similar model was recently used to study the approach of a liquid-coated sphere towards a layer of the same liquid [14].

Figure 1 shows the initial stages in the evolution of the interfacial shape and pressure distribution. The pressure rises under the falling droplet, and eventually the drop shape develops a dimple when it is at a distance $H = H^*$ from the surface, determined below. Subsequently, the pressure develops two maxima as the interfacial curvature steepens rapidly.

What sets H^*? The pressure in the gas must be sufficient to decelerate the falling liquid, locally, from velocity V to rest in order to deform the droplet. Hence $\rho_l h_{tt} \sim \rho_l V/\tau$, where $\tau^{-1} = V/H$ is the time scale the fluid is brought to rest. Equation (2) then implies that $P_{\text{gas}}/L \sim \rho_l V/\tau + \sigma/R/L$, where $L = \sqrt{RH}$ is the axial length scale. For the shape to deform, the gas pressure must dominate drop inertia and surface tension.

When the drop is far from the substrate, $\rho \approx \rho_0$, and the gas pressure is set by incompressible viscous drainage. Equation (1) then implies $P \sim \mu VR/H^2$. Assuming sufficiently weak surface tension, the gas pressure gradient balances the liquid deceleration. This gives the height

$H^* = RSt^{2/3}$ at which the droplet deforms, where $St = \mu/\rho_l VR$ is the Stokes number.

If the pressure in the gas, P_{gas}, becomes of order the ambient pressure before the drop can deform, the underlying gas compresses. This happens when $P_{\text{gas}} \sim P_0$, or when $H_* = R(\mu V/RP_0)^{1/2}$. Below this threshold height, (1) reduces to $(\rho h)_t \approx 0$ or $\rho h = \rho_0 H_*$, where ρ_0 is the initial gas density. Balancing the gas pressure gradient with the liquid deceleration then gives $H = RSt^{2/3}\epsilon^{(2-\gamma)/(2\gamma-1)}$, where $\epsilon \equiv P_0/(R\mu^{-1}V^7\rho_l^4)^{1/3}$. Identical scaling laws can also be derived for axisymmetric geometry.

We verified these scaling laws by simulating Eqs. (1) and (2) for a wide range of St and ϵ and tracked the height H^* when the shape of the interface first deviates from a spherical shape. At large ϵ, the film thickness obeys the incompressible scaling $H \sim RSt^{2/3}$, while as ϵ decreases, compressible effects set in and the dynamics cross over to the compressible scalings aforementioned. Figure 2 shows this crossover for both isothermal ($\gamma = 1$) and adiabatic ($\gamma = 7/5$) equations of state. The experimental splashing threshold [6] occurs in the compressible regime. The figure also shows contours of constant H^* as a function of V and P_0, corresponding to ethanol drops used by Xu, Zhang, and Nagel [6]. The solid dots denote their measured splash thresholds. The range of H^* spanned by the splashing threshold is from 200 nm to 2 μm, with thicker films for slower drops and larger ambient pressures.

If we rescale the film thickness h in Eqs. (1) and (2) by incompressible scaling $RSt^{2/3}$, x by $RSt^{1/3}$, ρ by ρ_0, and P by P_0, only two dimensionless parameters characterize the resulting dynamics: In addition to ϵ, we have $\delta \equiv \sigma/RP_0$ comparing surface tension to compressibility. For splashing, $\delta \sim 10^{-4}$ and is negligible in the absence of sharp curvatures. Hence we expect ϵ to be the only
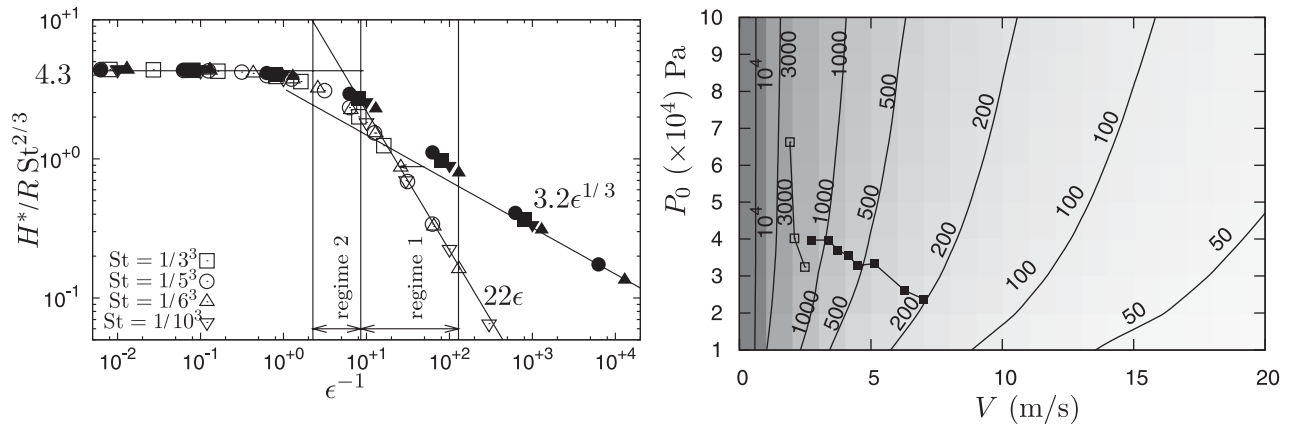

FIG. 2.   Dimple height H^* as a function of impact parameters. Left panel: H^* versus ϵ for a range of St. Open symbols denote $\gamma = 1$, while the corresponding filled symbols denote $\gamma = 1.4$. The data collapse onto a single curve, with asymptotes agreeing with the predictions. Regimes 1 and 2 correspond to the experiments of Xu, Zhang, and Nagel. Right panel: Contours of constant H^* in nm for ethanol drops of size corresponding to the experiments by Xu, Zhang, and Nagel using $\gamma = 1.4$ and a range of impact velocities V and gas pressures P_0. Filled squares denote regime 1 of threshold splashing curve observed by Xu, Zhang, and Nagel, while open squares denote their regime 2.

important parameter for the initial stages of droplet deformation.

Figure 1 shows that subsequent to initial interfacial deformation, the interface develops two symmetric kinks that move away from the origin, with the film thickness at the kink decreasing (h_{min}), and the maximum pressure p_{max} increasing with time. The characteristic x scale of the kink (l) rapidly decreases as $h_{min} \rightarrow 0$, causing the interfacial curvature to increase. Figure 3 shows p_{max} and l as a function of h_{min} for various values of ϵ. At high ϵ, we have $p_{max} \sim h_{min}^{-1/2}$ and $l \sim h_{min}^{3/2}$, whereas in the compressible regime at low ϵ there is an initial transient regime with $p_{max} \sim h_{min}^{-\gamma}$ and $l \sim h_{min}^{1+\gamma}$ before the aforementioned scaling laws take over.

We now construct an approximate analytical description for the leftmost kink, neglecting surface tension. The height and density fields are described by the similarity solution $h(x,t) = h_{min}(t)H(\eta)$ and $\rho(x,t) = \rho_{max}R(\eta)$, where $\eta = (x - Ut)/l(t)$ is the similarity coordinate, with $\rho_{max}(t)$ the maximum density and U the dimensionless speed of the kink, possibly depending on ϵ. To the
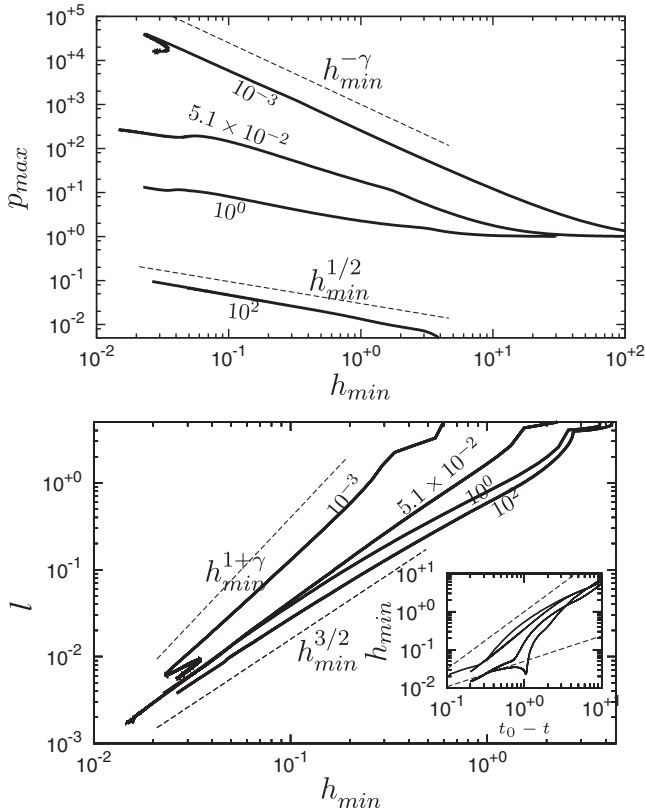

FIG. 3. Maximum pressure p_{max} (top) and curvature length scale l (bottom) as a function of h_{min} shown in solid lines. Labels denote values of ϵ. The ambient pressure is subtracted from p_{max} for $\epsilon = 100$. The dashed lines denote various power-law estimates (see text). The value $\epsilon = 5.1 \times 10^{-2}$ corresponds to Fig. 1 of Xu, Zhang, and Nagel [6]. The inset on the bottom shows h_{min} against $t_0 - t$, where t_0 is the time to contact.

right of the kink, the density is high and the gas is compressible; to the left of the kink the density relaxes to ambient and the pressure is determined by viscous stresses. The transition from compressible to incompressible behavior occurs at the kink and is advection dominated, i.e., $\partial_t \approx U\partial_x$. Substituting the similarity solutions in the dimensionless forms of (1) and (2) yields two dominant balances in three unknowns h_{min}, ρ_{max}, and l which can be solved and translated back to dimensional form to give

$$l \propto R \frac{U^{1/2}}{St^{2/3}}\left(\frac{h_{min}}{R}\right)^{3/2}, \qquad p_{max} \propto \frac{\mu V}{RSt}\left(\frac{RU^3}{h_{min}}\right)^{1/2}. \quad (3)$$

A similar analysis in the incompressible limit ($\epsilon \gg 1$) also reveals identical power laws for l and p_{max}, except here p must be interpreted as the perturbation about the ambient.

However, for small ϵ a different solution emerges in the initial stages of the compressible regime. These dynamics are then well captured by $\rho h = A + f(t)F(\eta) + \ldots$, where A is time independent and initially dominates the second term. This implies $\rho_{max} \propto 1/h_{min}$ and $p_{max} \propto 1/h_{min}^{\gamma}$. Equation (2) then implies in dimensional terms

$$l \propto R \frac{\rho_l U^2}{P_0}\left(\frac{RP_0}{\mu V}\right)^{\gamma/2}\left(\frac{h_{min}}{R}\right)^{1+\gamma},$$
$$p_{max} \propto P_0\left(\frac{RP_0}{\mu V}\right)^{\gamma/2}\left(\frac{h_{min}}{R}\right)^{-\gamma}. \quad (4)$$

Ultimately $f(t)$ becomes larger than A, causing a regime change to (3).

The solution thus described appears to support the notion that liquid-solid contact occurs entraining a gaseous bubble underneath. However, thus far we have ignored surface tension. Although initially unimportant, the interfacial curvature h_{min}/l^2 diverges more quickly than the gas pressure, leading to a crossover to a regime where surface tension is important. Figure 4 continues the simulation of Fig. 1 to this regime. The bottom panel shows that when the capillary pressure $\sigma \max(h_{xx})$ balances the gas pressure p_{max}, the behavior transitions to an entirely different regime. Snapshots of the droplet interface in the top panel demonstrate that instead of entraining a gaseous bubble and contacting the solid surface, liquid-solid contact is completely avoided. The pressure maximum saturates and becomes a source of capillary waves.

To estimate when this crossover occurs, we use the asymptotically valid power law, $l \propto h_{min}^{3/2}$. Balancing the gas pressure gradient with the capillary pressure gradient implies that the crossover occurs when $l \sim RSt^{5/3}/Ca$, where Ca is the capillary number $\mu V/\sigma$. The gas layer thickness scales as $h_{min} \sim RSt^{14/9}/Ca^{2/3}$, with the constant of proportionality determined from simulations to be about 2.54. For a 2 mm diameter water drop moving at 0.5 m/s, the scales are of order $l \sim 0.5\ \mu$m and $h_{min} \approx 170$ nm, respectively; both these scales get smaller with increasing V.
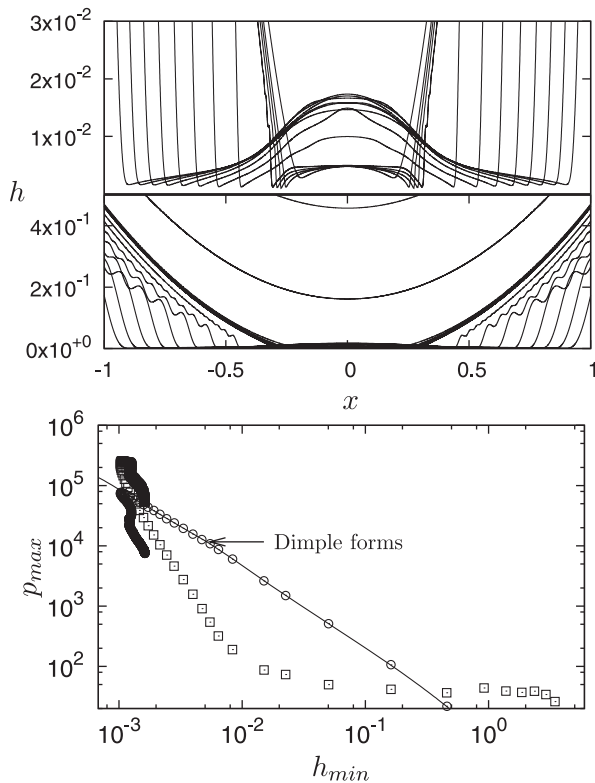
FIG. 4.   (Top) Evolution of a liquid droplet impacting a solid surface, with $\gamma = 1.4$ and $\epsilon = 5 \times 10^{-3}$, with surface tension $\delta = 20$. The interface no longer contacts the solid surface, and capillary waves are emitted. (Bottom) Gas pressure (circles) and capillary pressure (squares) as a function of h_{min}. h_{min} stops decreasing when gas pressure balances surface tension.

We have thus demonstrated that the nature of droplet impact on a solid surface is very different than has been assumed previously. Instead of parabolic point contact, the interface deforms substantially, being effectively decelerated to rest by the gaseous layer underneath. Although at high impact velocities, surface tension is initially irrelevant, squeezing the gaseous layer out near contact creates a kink. This kink moves at constant velocity and creates capillary waves. There is at least some precedent in the literature for our claim that liquid-solid contact is initially avoided because of an intervening air layer: In their studies of droplet bouncing on hydrophobic surfaces at velocities lower than the splashing threshold, Richard and Quéré [15,16] previously hypothesized the possibility of a thin film of air being trapped between the droplet and the solid substrate, though they were unable to observe it experimentally. To our knowledge, these calculations represent the first evidence explicitly documenting that the liquid drop does not contact the wall but instead spreads on a thin film of air, with a prediction for the film thickness. These conclusions are also applicable to a solid sphere impacting a liquid surface [17,18]. Our calculations neglect intermolecular attraction between the liquid and

solid, which will ultimately cause contact, albeit on a longer time scale [19].

Finally, with regards to splashing, the solution of (1) and (2) computed does not show any indication of splashing. Hence we are forced to conclude that other physical effects like viscosity of the drop liquid, mean-free path of the gas, and thermal and mass transfer should be included to obtain splashing behavior. These effects are initially negligible but can become important as the drop interface approaches the wall along the self-similar solution. In this Letter, we have demonstrated how to include the effects of surface tension, but the same technique can be used for these other physical effects. This approach allows for a systematic investigation of droplet impact under these different conditions.

*shreyas@seas.harvard.edu
[1] A. Worthington, Proc. R. Soc. London **25**, 261 (1876).
[2] Z. Levin and P. Hobbs, Phil. Trans. R. Soc. A **269**, 555 (1971).
[3] C. Stow and M. G. Hadfield, Proc. R. Soc. A **373**, 419 (1981).
[4] A. Yarin and D. Weiss, J. Fluid Mech. **283**, 141 (1995).
[5] M. Bussmann, S. Chandra, and J. Mostaghimi, Phys. Fluids **12**, 3121 (2000).
[6] L. Xu, W. W. Zhang, and S. R. Nagel, Phys. Rev. Lett. **94**, 184505 (2005).
[7] M. B. Lesser, Proc. R. Soc. A **377**, 289 (1981).
[8] J. E. Field, J. Dear, and J. E. Ogren, J. Appl. Phys. **65**, 533 (1989).
[9] K. Haller, D. Poulikakos, Y. Ventikos, and P. Monkewitz, J. Fluid Mech. **490**, 1 (2003).
[10] G. I. Taylor and P. G. Saffman, J. Aeronaut. Sci. **24**, 553 (1957).
[11] F. Smith, L. Li, and G. Wu, J. Fluid Mech. **482**, 291 (2003).
[12] W. H. Press, B. P. Flannery, S. A. Teukolsky, and W. T. Vetterling, *Numerical Recipes—The Art of Scientific Computing* (Cambridge University Press, Cambridge, England, 1986).
[13] T. Y. Hou, J. S. Lowengrub, and M. J. Shelley, J. Comput. Phys. **114**, 312 (1994).
[14] A. A. Korobkin, A. S. Ellis, and F. T. Smith, J. Fluid Mech. **611**, 365 (2008).
[15] D. Richard and D. Quéré, Europhys. Lett. **50**, 769 (2000).
[16] Y. Renardy *et al.*, J. Fluid Mech. **484**, 69 (2003).
[17] S. T. Thoroddsen, T. G. Etoh, K. Takehara, and Y. Takano, J. Fluid Mech. **499**, 139 (2004).
[18] C. Duez, C. Ybert, C. Clanet, and L. Bocquet, Nature Phys. **3**, 180 (2007).
[19] Y. Couder, E. Fort, C.-H. Gautier, and A. Boudaoud, Phys. Rev. Lett. **94**, 177801 (2005).